Received: 9 December 2023 | Revised: 22 December 2023 | Accepted: 2 January 2024
DOI: 10.1002/pc.28127

RESEARCH ARTICLE

Polymer COMPOSITES WILEY

On the energy absorption in a novel CoFeSiB metallic-glass fiber/epoxy resin composite under quasi-static and dynamic compression conditions

Weizhong Liang[1] | **Longxing Wang**[1] | **Peter K. Liaw**[2] | **Yingyi Liu**[1] | **Ransong Wei**[1] | **Jiawen Xu**[1]

[1]School of Materials Science and Engineering, Heilongjiang University of Science and Technology, Harbin, People's Republic of China

[2]Department of Materials Science and Engineering, University of Tennessee, Knoxville, Tennessee, USA

Correspondence
Weizhong Liang, Yingyi Liu, and Jiawen Xu, School of Materials Science and Engineering, Heilongjiang University of Science and Technology, Harbin 150022, People's Republic of China.
Email: wzliang1966@126.com, liuyingyi_hit@163.com, and xujiawen@sina.com

Funding information
National Natural Science Foundation of China, Grant/Award Numbers: 52171155, 1611180, 1809640, 2226508

Abstract

Manufacturing and investigating metallic-glass-fiber-reinforced epoxies is an important new attempt to present their potential to contribute to the aviation industry. In order to explore the energy absorption in novel CoFeSiB metallic-glass-fiber/epoxy resin composites, CoFeSiB/epoxy resin composite cylinders with different fiber volume fractions were prepared by a hot-pressing method. The amorphism of the metal fibers was analyzed using x-ray diffraction. The quasi-static compression tests were performed on different fiber oriented samples with a diameter of 3.6 mm and a height of 7.2 mm. The sample with the fiber orientation [0°/90°] has a higher energy absorption capacity, compared to the one with the fiber orientation [0°/0°]. The dynamic- compression tests were performed on the [0°/0°] samples with a diameter of 3 mm and height of 6 mm at different air pressures. The compression fracture surfaces were examined by scanning electron microscope. Then the energy absorption mechanism of the composites was investigated. This study is of great significance for the energy absorption in amorphous metal fiber/epoxy composites.

KEYWORDS
composites, energy absorption, epoxy, metallic-glass fiber

1 | INTRODUCTION

Bulk-metal glasses (BMGs) have wide structural applications due to their high strength, high hardness, and good corrosion resistance. But they lack room temperature plastic deformation ability, which greatly limits their application in engineering materials.[1–10] The deformation behavior of BMGs visibly relies on the size effect, with the smaller sample presenting higher plasticity.[11,12] Therefore, metallic-glass-fiber (MGF) has received extensive attention because micro- or nanoscale MGF has high strength and better plasticity.[13] Wang[14] studied the tensile behavior of a Co-based MGF after cold pulling and found that its tensile strength reached 4000 MPa and its plasticity was up to 1.6%. Yi[15] prepared $Pd_{40}Cu_{30}Ni_{10}P_{20}$ metal-glass nanoscale fiber and revealed that the smaller MGF showed superior tensile plasticity. Zberg[16] studied the tensile property of the MgZnCa MGF, and Weibull Statistical methods were used to analyze its reliability. It was suggested that a smaller diameter promoted the tensile plastic-deformation behavior of the studied MGF. Due to its excellent mechanical properties, MGF is a hopeful material for potential structural applications in micro/nano-electro-mechanical systems.[10,17,18]

Composite materials have advantageous performances owing to the unique superiority of the component materials.[19,20] Fiber reinforced composites are widely used in the electronics, machinery manufacturing industry, automobile, and aerospace fields because of their low density, low thermal conductivity, high specific strength, corrosion, and fatigue resistance.[21–29] Epoxy resin is a commonly used matrix in fiber reinforced composites at medium temperatures for its excellent corrosion resistance and high chemical stability.[21,30,31] MGF may be used as the enhanced phase in the epoxy-resin matrix for its low density, high strength, and good corrosion resistance.[32]

So far, no study has been found on the energy absorption in novel CoFeSiB MGF/epoxy resin composites, although carbon-fiber or steel-reinforced resin-epoxy composite have presented energy absorption characteristics. For example, Ryzińska[33] investigated the effect of fiber architecture on the specific energy absorption in carbon-epoxy composite tubes under progressive crushing. It was found that the amount of energy absorbed of the composite tube increased by 76% with the axial fiber mass fraction increasing from 0.5 to 1. Xiong[34] studied the compression behavior and energy absorption of a carbon-fiber/epoxy resin composite sandwich panel made of three-dimensional (3D) honeycomb grid cores. The results showed that the 3D grid core sandwich panels exhibited higher absorption capacity, compared to other square honeycombs. In this paper, the effects of fiber contents, fiber orientations, and air pressure on the energy absorption of the new CoFeSiB MGF/epoxy resin composites were investigated by compression experiments. The mechanism of energy absorption of the novel composites was analyzed from the failure mode and the morphology of compression surfaces.

2 | MATERIALS AND METHODS

2.1 | Materials and samples

The $Co_{68}Fe_5Si_{12}B_{15}$ (atomic percent, at.%) button ingot was prepared by arc-melting mixtures of the elements (Co, Fe of 99.99% in purity and Si, B of 99.9% in purity weight percent) in a Ti-gettered argon atmosphere. The button ingot was melted six times, and followed by suction-casting into a copper mold to produce a cylindrical rod with a diameter of 10 mm and a length of 70 mm. To form MGF, the rod was remelted and subsequently extracted in a home-made melt-extracted device. The details of the MGF preparation have been illustrated in Reference 17. The average diameter range of the resulting MGF with a smooth surface is between 30 μm and 50 μm, which is shown in Figure 1. The used epoxy resin was composed of E-20 and E-51 mixing matrix, dicyandiamide 100 S curing agent and 1.2-dimethylimidazole promoter in a ratio of 50:50:7:1, provided by a commercial corporation.

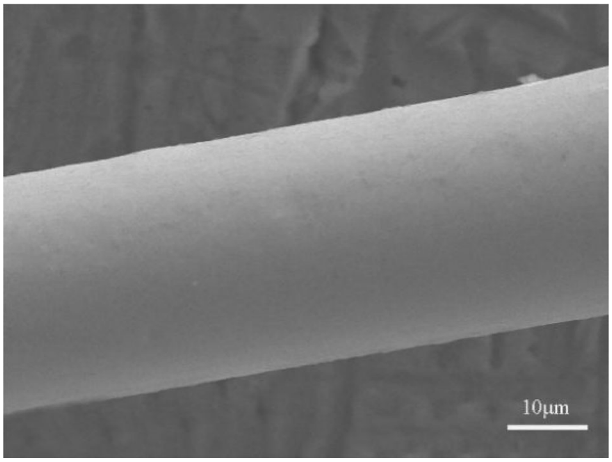

FIGURE 1 Scanning electron microscope image of $Co_{68}Fe_5Si_{12}B_{15}$ MGF.

The $Co_{68}Fe_5Si_{12}B_{15}$ MGF/epoxy resin composites were prepared by a prepreg two-step vacuum hot pressing method. A MGF sheet was first laid out by hand with a nominal ply thickness of 0.08 mm, length of 45 mm, and width of 40 mm, and then 40% ± 2% epoxy resin was uniformly coated on the surface of the fiber sheet. After the excess resin was removed from these fiber sheets, the coated fibers were equably placed in a cylindrical graphite mold along the longitudinal direction to form prepregs stored in a refrigerator. The refrigerated prepregs were subsequently placed in a vacuum bag under 0.5 MPa, first heated to 108°C for 30 min, and then heated to 133°C for 30 min to cure the cylindrical composites.

Type-A samples with a diameter of 3.6 mm and a height of 7.2 mm were directly cut from the composite cylinders with fiber volume fractions of 50%, 60%, and 70%, denoted as samples A1, A2, and A3, respectively. Type-B samples with the same size and fiber volume fraction as sample A2 mentioned above were made up of different height composite cylinders glued together, denoted as samples B1, B2, B3, and B4, respectively, as shown in Figure 2A–D. Type-A and B samples were used for static compression tests. Type-C samples with a diameter of 6 mm and a height of 3 mm used for the dynamic test were cut from the composite cylinders with a fiber volume fraction of 60%.

2.2 | Experimental methods

The microstructure of the extracted $Co_{68}Fe_5Si_{12}B_{15}$ fiber was analyzed by an x-ray diffractometer (XRD) with Cu K_α radiation. Figure 3 shows the XRD pattern of the used

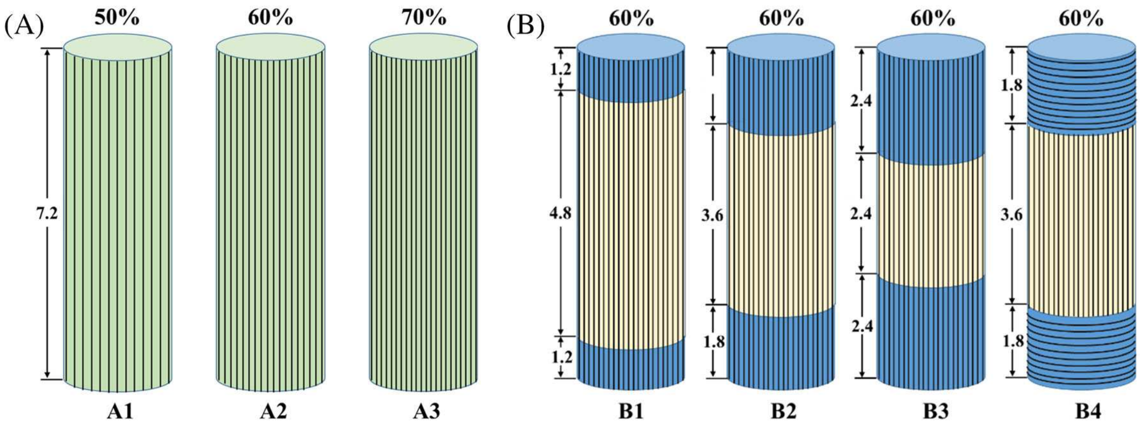

FIGURE 2 Type-A (A) and Type-B (B) samples with different fiber orientations diagrams.

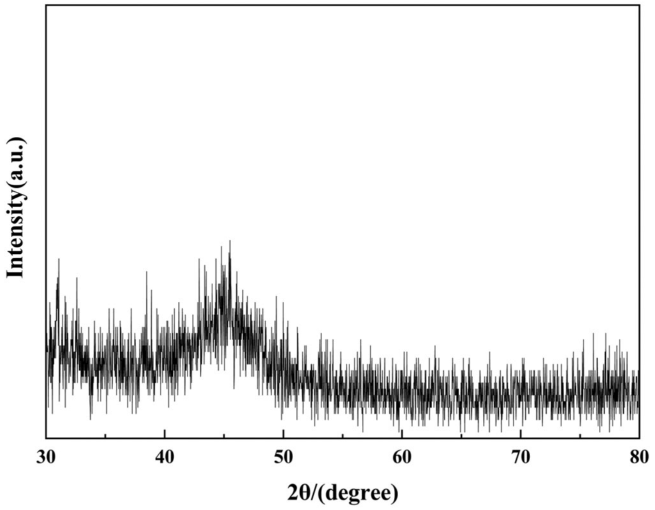

FIGURE 3 X-ray diffractometer pattern of $Co_{68}Fe_5Si_{12}B_{15}$ MGF.

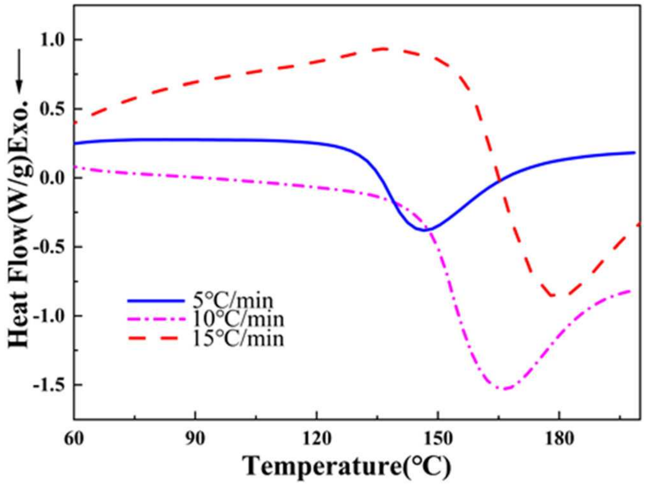

FIGURE 4 Differential scanning calorimeter curves of the used epoxy resin at different heating rates.

TABLE 1 The relationships among the air pressure, impact speeds and strain-rates.

Air pressure (MPa)	0.5	0.3	0.2
Impact speed (m/s)	15.66	12.01	8.47
Strain-rate (s^{-1})	6140	4312	2684

MGF without crystal sharp peak characteristics. The thermal effect of the used epoxy resin was researched, using a differential scanning calorimeter (DSC) in a flow of pure nitrogen gas at a constant heating rate of 5, 10, and 15 K min^{-1}, respectively. Figure 4 shows the DSC curves of the epoxy resin at three heating rates with a single exothermic peak. The curing temperature of the epoxy resin was determined by linear-fitting characteristic temperatures on the DSC curves of the above three heating rates.

Composite cylindrical samples were tested under quasi-static and dynamic compressive loading at room temperature. The quasi-static compressive tests were performed on an INSTRON 5505R at a loading rate of 0.1 mm/min. The preload is 0.05 kN. A split Hopkinson pressure bar (SHPB) was used for dynamic-compression testing at 0.2, 0.3, and 0.5 MPa air pressure, respectively. The relationships among the air pressure, impact speed, and strain-rate are given in Table 1. The fracture morphologies of the samples were observed by a scanning electron microscope (SEM), and the failure modes of the composites were analyzed.

The longitudinal compressive strength formula can be obtained, using the energy method and mixing law and is expressed as,[35]

$$\sigma_{\overline{c/u}} = \sigma_{\overline{\mathrm{mcr}}}\left[1+\left(\frac{E_{\mathrm{f}}}{E_{\mathrm{m}}}-1\right)V_f\right], \tag{1}$$

where $\sigma_{\overline{\mathrm{mcr}}}$ is the critical stress of the matrix when the shear instability occurs, E_{f} is the elastic modulus of the

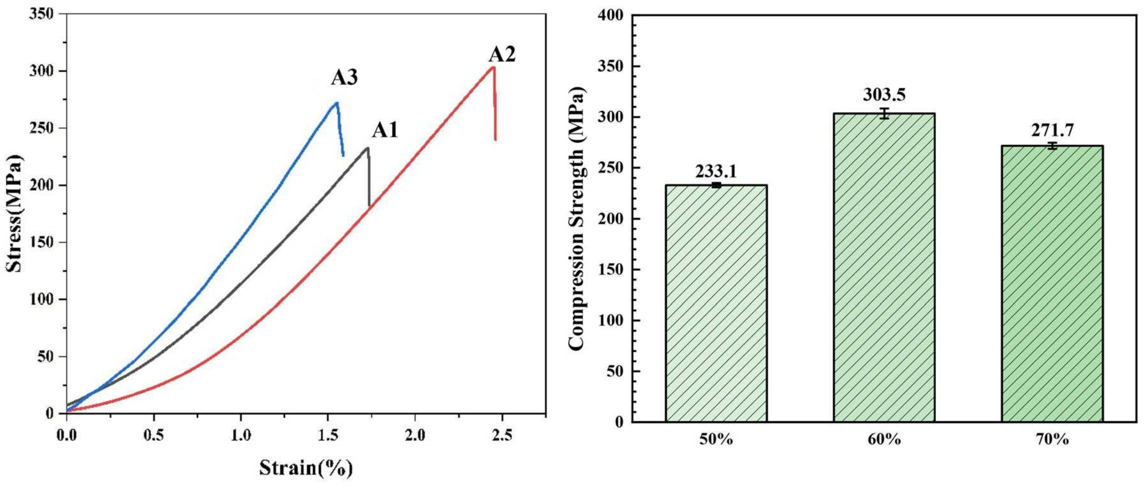

FIGURE 5 Compression stress–strain curves of Type-A samples with different fiber volume fractions.

fiber, E_m is the elastic modulus of the matrix, V_f is the fiber volume fraction.

The energy absorption can be calculated by integrating the compression stress–strain curve and is described as.[36]

$$w = \int_0^{\varepsilon_D} \sigma(\varepsilon) d\varepsilon, \tag{2}$$

where w is the specific energy absorbed, $\sigma\,(\varepsilon)$ is the compression stress, and ε_D is the compression strain.

3 | RESULTS AND DISCUSSION

3.1 | Static compression responses

Figure 5 shows the compression stress–strain curves of Type-A samples with fiber volume fractions of 50%, 60%, and 70% under a quasi-static test condition. Owing to the consistency of the experimental results, only one curve for each fiber oriented structure is shown in the graph for clarity. As can be seen from Figure 5, the strength of all peaks is followed by a lower stress state when the fiber volume fraction increases from 50% to 70%. The peak strengths of samples A1, A2, and A3 increase first and then decrease, which are 233.1, 303.5, and 271.7 MPa, respectively. The difference in the energy absorption of different fiber volume fractions is evident from the stress–strain curves of the peak strength.

Type-A samples presented a similar crushing mode, the cylinders were pressed into frustum cone-like "cups." By observing the surface of "cups," it is able to distinguish the difference in the morphology of samples with different fiber volume fractions, as shown in Figure 6. In sample A1, the MGFs were separated from the epoxy resin, and the composite material presented severe interlayer splitting. For sample A2, the MGFs were closely arranged and well combined with the epoxy resin, and interlaminar splitting occurred in a few parts. The MGFs in sample A2 played the main role in load transfer and suffered from greater pressure. So, sample A2 showed good load-carrying capacity. For the sample A3, the MGFs were poorly bonded to the epoxy resin, and there was obvious stratification between the fiber and the matrix. Therefore, the MGFs were unable to withstand greater stresses, resulting in a decrease of the compressive strength. In summary, the sample with a fiber volume fraction of 60% possessed a larger energy absorption capacity.

Figures 7 and 8 show compression stress–strain curves and sample shape after the compression failure of the Type-B samples with different fiber oriented structures. The compressive behavior of all Type-B samples can be roughly divided into three stages, the initial failure stage, the smooth failure stage, and the final failure stage in Figure 7. Type-B samples presented a different degree of crushing mode than the type-A samples, the cylinders were gradually flattened and exhibited interlayer splitting and fell off, as shown in Figure 8. Samples B1, B2, and B3 entirely reach an initial peak intensity in the range of 0% to 5% strain (see Figure 7A). After sample B1 reaches the peak intensity of 127.5 MPa, it starts to lose strength, and then successively enters the smooth failure stage with slowly decreasing strength and the final failure stage with slightly increasing strength (Figure 7A(E1-1,E1-2)). The MGFs deflected during the compression process, some fibers separated from the resin at the interface, and some fibers were pulled out (Figure 8A). As the strain continued to increase, the sample B1 became flattened and entered the final failure stage with an axial splitting mode (Figure 8B). Compared with sample B1, the peak

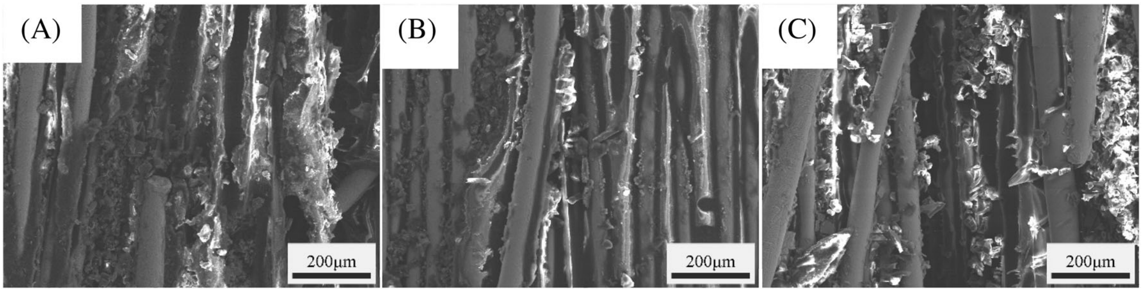

FIGURE 6 Morphologies of side surfaces of Type-A samples with different fiber volume fractions after compression by SEM, (A) A1-50%, (B) A2-60%, and (C) A3-70%.

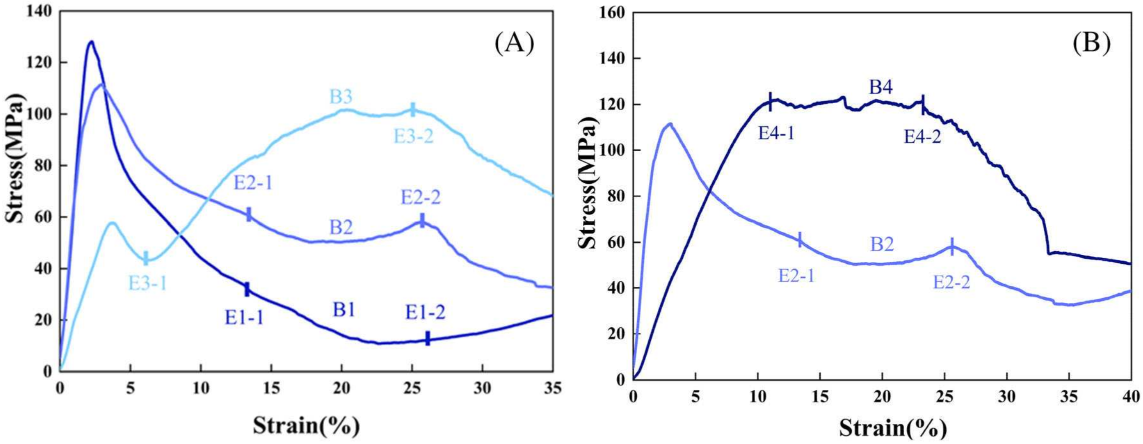

FIGURE 7 Compression stress–strain curves of Type-B samples with different fiber orientations, (A) B1, B2, and B3 and (B) B2, B4.

strength of sample B2 in the initial failure stage is reduced to 110.4 MPa. The strength values of the sample B2 in the smooth failure stage and the final failure stage are overall higher (Figure 7A(E2-1,E2-2)), indicating large energy absorption. During the smooth failure stage, the fiber offset angle of sample B2 increased, and the fiber became more entangled (Figure 8C). As the strain continued to increase, sample B2 also entered the final failure stage with an axial splitting mode (Figure 8D). The peak strength of the sample B3 in the initial stage continues to decrease, which is 57.5 MPa. However, the strength values of the sample B3 in the smooth failure stage and the final failure stage are mostly higher (Figure 7A(E3-1,E3-2)), and the maximum value is 101.8 MPa, indicating greater energy absorption. With the strain increasing, the upper part of the sample B3 fell off (Figure 8E), and the middle one was pressed to the 90° off axis, entering the final failure stage (Figure 8F). In general, with the decreasing size of middle fiber in the Type-B samples, the compressive strength of the samples decreased and their damage increased. Due to the fiber damage from winding to interlaminar splitting to deflecting, the energy absorption capacity of the new material increased.

Samples B2 and B4 have the same length of middle fiber but different fiber orientation structures. The compression stress–strain curves are compared in Figure 7B. The compression strength of the sample B4 increases first, then remains basically unchanged, and finally decreases. Compared with sample B2, the compression strength of sample B4 is relatively high, reaching 122.59 MPa. Between 10% and 25% strains, sample B4 has a large plastic platform and exhibits good energy absorption capacity (Figure 7B(E4-1)). With increasing strain, the compressive strength of the sample B4 decreases and enters the final failure stage (Figure 7B(E4-2)). During the compression process, the upper part and the middle one of the sample B4 were split and inclined at a large angle to both sides (Figure 8G), some fibers became entangled, and part of the fibers was pulled out (Figure 8H), indicative of a more serious damage state.

3.2 | Dynamic compression responses

Figure 9 shows the dynamic compression stress–strain curves of Type-C samples at 0.2, 0.3, and 0.5 MPa air pressures. As can be seen from the dynamic stress–strain

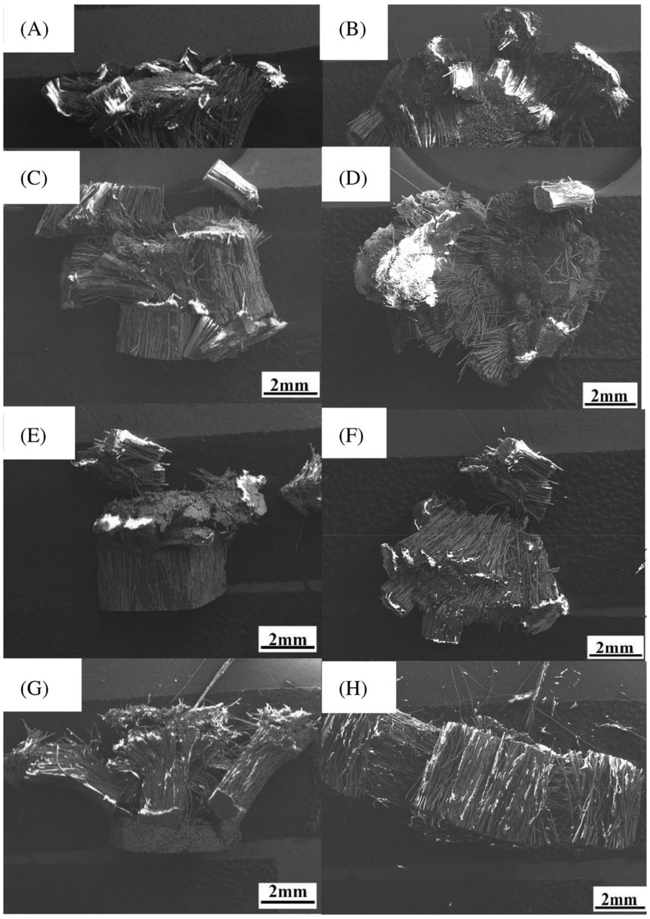

FIGURE 8 Scanning electron microscope images of compression surface of Type-B samples with different fiber orientations, (A, B) B1, (C, D) B2, (E, F) B3, and (G, H) B4.

curve at a 0.5 MPa air pressure in Figure 9A, when the strain is between 0% and 0.85%, the stress increases first, and then decreases. This is because the fibers in the sample underwent elastic deformation due to the low stress in the initial stage of compression. Moreover, under dynamic-compressive stress, this elastic deformation will undergo hysteresis, resulting in a reverse increase in stress. As the strain continues to increase, the dynamic-compressive stress increases rapidly in a short time. When the strain increases to 3.25%, the compressive strength reaches the peak value of 279.7 MPa, and then the compressive strength decreases after the material failure. Figure 9B,C show the dynamic-compressive stress–strain curve at 0.3 MPa and 0.2 MPa air pressures, respectively. Compared with Figure 9A, the compressive stress in the sample also increases first, and then decreases when the strain is between 0% and 0.35% at a 0.3 MPa air pressure and between 0% and 0.25% at a 0.2 MPa air pressure. This result showed that the elastic deformation of the metal glass fiber could resist the impact on the sample surface exerted by the incident rod at the initial stage and kept the stress change low in a small strain region. As the strain continues to increase, the compressive stress in the sample increases. When the compressive strain is 1.72% and 1%, the compressive strength of the sample reaches the peak values of 186.7 MPa (0.3 MPa air pressure) and 152.9 MPa (0.2 MPa air pressure), respectively. Then the MGF/epoxy resin composites fail, and the strength gradually decreases. These results are consistent with the experimental results published by Jia[26] for carbon-fiber/epoxy composites. A platform appears in the strain range of 3.5%–4% (Figure 9B) or in the strain range of 1.35%–1.54% (Figure 9C), indicating that the fibers would store part of the elastic deformation, which inhibited the reduction of the dynamic-compressive stress in the sample.

Figure 10 shows images of the Type-C sample after the dynamic-compression test at 0.2, 0.3, and 0.5 MPa air pressures. The sample was obviously collapsed at a 0.2 MPa air pressure in Figure 10A, and the bottom of the sample fractured. The fiber on the upper end is relatively complete, and there is a wide crack in the middle region (Figure 10B). Compared with the sample under 0.2 MPa pressure, the sample under 0.3 MPa pressure was seriously damaged. The cracks in the bottom of the sample increased, and some fibers fell off. There are also large cracks in the middle area of the sample, as shown in Figure 10C. The sample was compressed more seriously under 0.5 MPa air pressure. The fibers were basically offset, and the interface between the fibers and the resin was separated, as shown in Figure 10D. The bottom of the sample was basically crushed, and the fiber spalling appeared at the edge of the sample, as shown in Figure 10E. Due to the increase in air pressure, the impact force of the incident rod increased, and the surface of the sample was compacted. The upper fibers were separated from the resin, and the fibers were bent, as shown in Figure 10F.

3.3 | Composite failure mode

All Type-A, B1, B2, and B3 samples having a fiber orientation [0°/0°] were pressed in the direction of the fiber during the compression process, and the fibers were kept in a straight line. Under the action of pressure, the fibers maintained a certain anti-compression capacity. When the epoxy matrix reached the shear instability limit, the matrix lost its ability to prevent deformation. Therefore, samples of Type-A, B1, B2, and B3 were destroyed by overall compression, which began with transverse tensile cracking and followed shear deformation.

The longitudinal compressive strength of unidirectional metal glass fiber/epoxy resin composites is determined by the buckling of the epoxy resin matrix. From Formula (1), it can be seen that the larger the fiber volume fraction, the

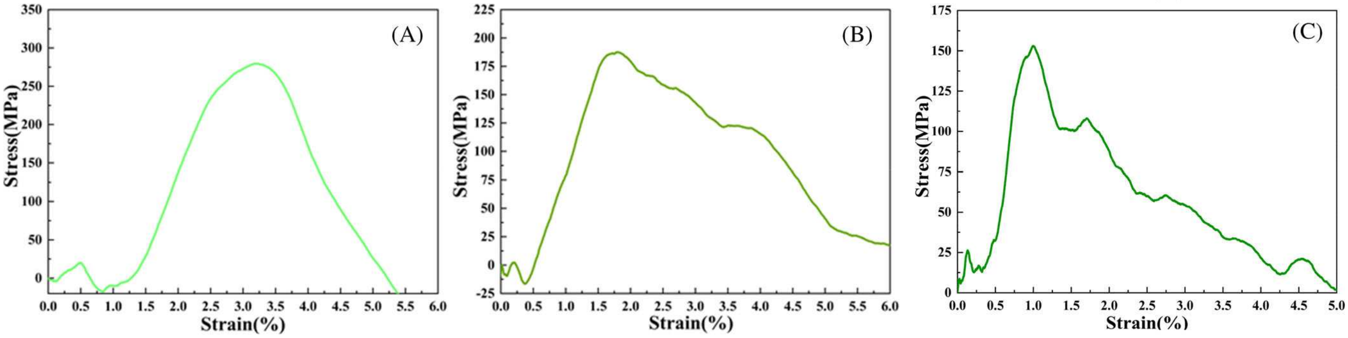

FIGURE 9 Dynamic-compression stress–strain curves of Type-C samples at different air pressures, (A) 0.5 MPa, (B) 0.3 MPa, and (C) 0.2 MPa.

higher the longitudinal compression strength. However, when the fiber volume fraction exceeds a certain limit, fiber degumming occurs, and the fiber cannot withstand greater stress, resulting in a reduction of the mechanical properties of sample A3.

In the compression process of sample B4 with a fiber orientation [0°/90°], the top and bottom were subjected to transverse compression, and the middle one was subjected to longitudinal compression. Under the transverse compressive load, the failure of the top and bottom was caused by the shear failure of the matrix, accompanied by fibers degumming and deformation. The failure of the middle part was caused by the transverse tensile cracking of the matrix, followed by shear deformation, also accompanied by fibers degumming and deformation.

In the process of dynamic compression, all the Type-C samples exhibited a similar crushing mode. Due to the difference of air pressure, the velocity of the incident rod is different, and the impact force of the incident rod on the sample is also different. With the increase of the air pressure, the crushing damage to the sample was more serious. Due to the low strength and poor plasticity of the resin, the resin first cracked, then the fibers shifted, and finally the sample was crushed.

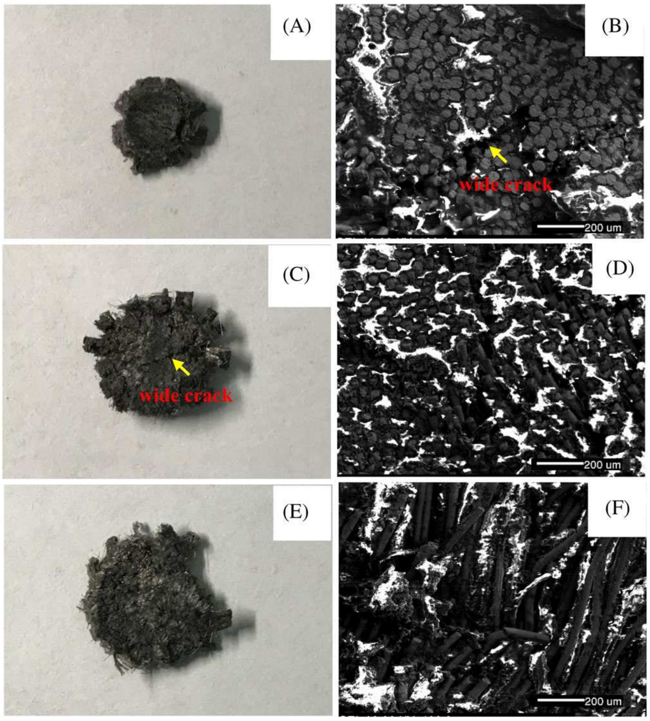

FIGURE 10 Images of compression surface of Type-C samples under different air pressures. (A, B) 0.2 MPa, (C, D) 0.3 MPa, and (E, F) 0.5 MPa.

3.4 | Energy absorption

The energy absorption of MGF/epoxy resin composites, calculated by Formula (2), can be reflected by the compressive stress–strain curve, as shown in Figures 7 and 9.

Figure 11 gives an energy absorption diagram of all Type-B samples with different fiber orientations. It shows that the energy absorption of samples B1, B2, B3, and B4 gradually increase, which are 33.6, 253.2, 601.4, and 1441.5 kJ/m^3, respectively. The energy absorption of sample B4 with a fiber orientation [0°/90°] is obviously the highest among all samples.

The compression behavior of samples B1, B2, B3, and B4 due to different architectures translates into different contributions of the failure mode and, consequently, to the amount of energy absorption.[31] By analyzing the degree of the middle part axial splits, and the mode of the top failure, it is found that different compressive zone morphologies lead to different amounts of energy absorption. With decreasing the middle part size of the samples B1, B2, and B3 with a fiber orientation [0°/0°], the ability of the fiber to maintain a straight line enhanced, the ultimate

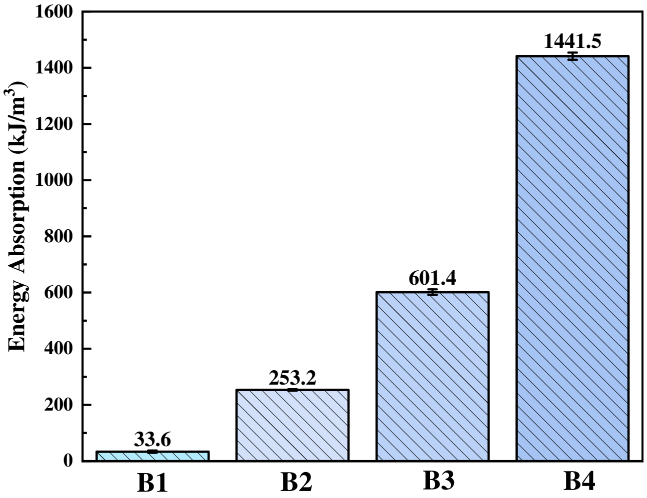

FIGURE 11 Energy absorption diagram of Type-B samples with different fiber orientations.

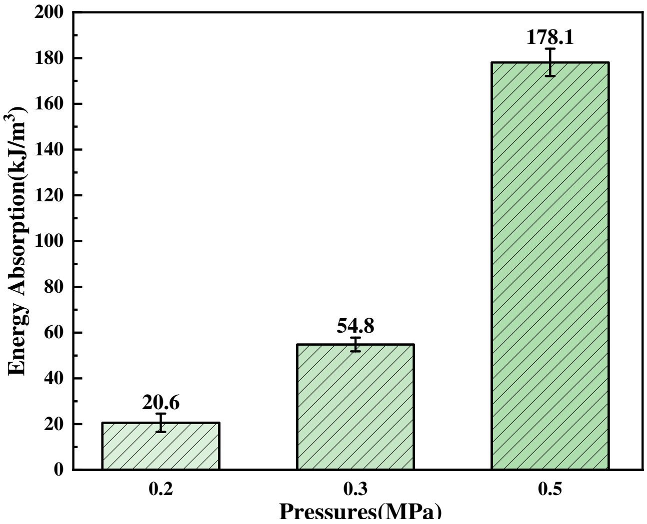

FIGURE 12 Energy absorption diagram of Type-C samples under different air pressures.

strength of the matrix shear instability increased, and the failure resistance of the composites structure increased. Hence, the energy absorption of the new material gradually increased. The B4 samples with a fiber orientation of [0°/90°] showed failures such as upper and lower shear fracture, central tensile fracture, fiber compression buckling, and debonding under compressive loading. This indicates that the energy absorption is larger than that of the samples with fiber orientation of [0°/0°] due to the presence of transverse shear fracture. Therefore, the samples with a fiber orientation [0°/90°] have more energy absorption than the ones with fiber orientation [0°/0°].

Figure 12 shows the energy absorption of Type-C samples at 0.2, 0.3, and 0.5 MPa air pressures. It can be seen that the energy absorption of Type-C samples continues to increase with an increase in the air pressure, which are 20.6, 54.8, and 178.1 kJ/m^3, respectively. The higher the air pressure, the more energy the Type-C sample absorbs, which can be justified by the level of damage to the sample at different air pressures (Figure 10A,C,E). In the process of dynamic-compression, due to the increase of the air pressure, the impact force of the incident rod on the sample increases, the density of the sample increases (Figure 10B,D,F), and the ability to resist the deformation behavior of the material is enhanced. So, the energy absorbed by the MGF/epoxy resin composite increases.

4 | CONCLUSIONS

An experimental study of a novel CoFeSiB MGF/epoxy resin composite on energy absorption has been performed under quasi-static and dynamic compression conditions. Three fiber contents, two fiber orientations and three air pressures were tested.

The greatest failure strength in the quasi-static and dynamic compression processes of samples was obtained for the fiber volume fraction of 60% and for the air pressure of 0.5 MPa, respectively. As the fiber volume fraction increases, the failure strength value decreases for the quasi-static test. The failure strength decreases with the increase in air pressure for the dynamic test.

The energy absorbed by the samples indicated that the sample with the fiber orientation [0°/90°] has more absorption capacity than the one with the fiber orientation [0°/0°] under quasi-static compression conditions. For the same fiber orientation [0°/0°], the energy absorbed by the sample increased with the increase of the air pressure from 0.2 to 0.5 MPa in a dynamic test. However, it increased with the decrease in fiber length of the middle part from 4.8 to 2.4 mm in a quasi-static test. The analysis of the relationship among the morphology of the compressive zone, failure mode, and energy absorption showed that the more serious the damage degree of the matrix and fiber, the more failure modes, and the greater the energy absorption.

ACKNOWLEDGMENTS

The present work is supported by the National Natural Science Foundation (Grant number 52171155). PKL very much appreciates the support from the National Science Foundation (DMR—1611180, 1809640, and 2226508).

DATA AVAILABILITY STATEMENT

The raw/processed data required to reproduce these findings cannot be shared at this time as the data also forms part of an ongoing study.

REFERENCES

1. Qu RT, Volkert CA, Zhang ZF, Liu F. Yield strength of "brittle" metallic glass. *J Mater Sci Technol*. 2023;149:247-254. doi:10.1016/j.jmst.2022.12.017
2. Gao K, Zhu XG, Chen L, et al. Recent development in the application of bulk metallic glasses. *J Mater Sci Technol*. 2022; 131:115-121. doi:10.1016/j.jmst.2022.05.028
3. Tantavisut S, Lohwongwatana B, Ittiravivong P, et al. The novel toxic free titanium-based amorphous alloy for biomedical application. *J Mater Res Technol*. 2018;7:248-253. doi:10.1016/j.jmrt.2017.08.007
4. Zhou J, Wang QQ, Zeng QS, Wang AD, et al. A plastic FeNi-based bulk metallic glass and its deformation behavior. *J Mater Sci Technol*. 2021;76:20-32. doi:10.1016/j.jmst.2020.11.016
5. Christopher AS, Todd CH, Ramamurty U. Mechanical behavior of amorphous alloys. *Acta Mater*. 2007;55:4067-4109. doi:10.1016/J.ACTAMAT.2007.01.052
6. Jiang H, Shang TT, Xian HJ, et al. Structures and functional properties of amorphous alloys. *Small. Struct*. 2021;2:2000057. doi:10.1002/sstr.202000057
7. Gargarella P, Pauly S, Song KK, et al. Ti-Cu-Ni shape memory bulk metallic glass composites. *Acta Mater*. 2013;61:151-162. doi:10.1016/j.actamat.2012.09.042
8. Hu WH, Yu ZJ, Lu YZ, et al. Enhanced plasticity in laser additive manufactured Nb-reinforced bulk metallic glass composite. *J Alloys Compd*. 2022;918:165539. doi:10.1016/j.jallcom.2022.165539
9. Jiang SD, Wang H, Sun JF, et al. Effect of strain rate on tensile behavior in amorphous fibers by an in-situ video extensometer system. *Mater Sci Eng A*. 2020;782:139252. doi:10.1016/j.msea.2020.139252
10. Yin H, Huang YJ, Xue P, Tong X, et al. Atomic structure evolution of high-entropy metallic glass microwires at cryogenic temperature. *Scr Mater*. 2019;163:29-33. doi:10.1016/j.scriptamat.2018.12.031
11. Huang YJ, Shen J, Sun JF. Bulk metallic glasses: smaller is softer. *Appl Phys Lett*. 2007;90:81919. doi:10.1063/1.2696502
12. Hussain I, Tong X, Wang G, et al. Cooling rate-dependent yield behavior of metallic glass wires. *Mater Sci Eng A*. 2017;683:236-243. doi:10.1016/j.msea.2016.12.022
13. Magagnosc DJ, Kumar G, et al. Effect of ion irradiation on tensile ductility, strength and fictive temperature in metallic glass nanowires. *Acta Mater*. 2014;74:165-182. doi:10.1016/j.actamat.2014.04.002
14. Wang H, Xing DW, Peng HX, Qin FX, Sun JF, et al. Nanocrystallization enabled tensile ductility of Co-based amorphous microwires. *Scr Mater*. 2012;66:1041-1044. doi:10.1016/j.scriptamat.2012.02.020
15. Yi J, Lewandowski JJ. Sample size and preparation effects on the tensile ductility of pd-based metallic glass nanowires. *Acta Mater*. 2015;87:1-7. doi:10.1016/j.actamat.2014.12.039
16. Zberg B, Arata ER, Löffler JF, et al. Tensile properties of glassy MgZnCa wires and reliability analysis using Weibull statistics. *Acta Mater*. 2014;57:3223-3231. doi:10.1016/j.actamat.2009.03.028
17. Su S, Yang T, Wang K, et al. Effect of strain rate on fracture reliability of $Cu_{45}Zr_{45}Co_{10}$ amorphous alloy microwires by statistical analysis. *J Alloys Compd*. 2022;898:162951. doi:10.1016/j.jallcom.2021.162951
18. Alekhina I, Kolesnikova V, Makarova L, Rodionova V, Perov N, et al. Radial dependence of circular magnetic permeability of amorphous magnetic microwires. *J Magn Magn Mater*. 2021;537:168155. doi:10.1016/j.jmmm.2021.168155
19. Qiao YJ, Yao ZD, Ji Y, et al. Preparation and microwave absorption of CIP/EP hollow spheres lattice composites. *Compos Part A Appl Sci Manuf*. 2021;150:106626. doi:10.1016/j.compositesa.2021.106626
20. Qiao YJ, Li QW, Li Q, et al. Improving thermal insulation properties of lightweight epoxy resin matrix composites with millimeter-sized hollow glass microspheres/epoxy hollow spheres. *Energ Buildings*. 2022;277:112546. doi:10.1016/j.enbuild.2022.112546
21. Zhang H, Wu K, Xiao G, Du Y, et al. Experimental study of the anisotropic thermal conductivity of 2D carbon-fiber/epoxy woven composites. *Compos Struct*. 2021;267:113870. doi:10.1016/j.compstruct.2021.113870
22. Soutis C. Fibre reinforced composites in aircraft construction. *Prog Aerosp Sci*. 2005;41:143-151. doi:10.1016/j.paerosci.2005.02.004
23. Chauhan V, Kärki TA. Review of natural fiber reinforced engineering plastic composites, their applications in the transportation sector and processing techniques. *J Thermoplast Compos Mater*. 2019;35:1169-1209. doi:10.1177/0892705719889095
24. Kausar A. Advances in carbon fiber reinforced polyamide-based composites materials. *Adv Mater Sci*. 2019;19:67-82. doi:10.2478/adms-2019-0023
25. Naser MZ, Hawileh RA, Abdalla JA. Fiber-reinforced polymer composites in strengthening reinforced concrete structures: a critical review. *Eng Struct*. 2019;198:109542. doi:10.1016/j.engstruct.2019.109542
26. Jang JU, Park HC, Khil MS, et al. Electrically and thermally conducutive carbon fiber fabric reinforced polymer composites based on nanocarbons and an in-situ polymerizable cyclic oligoester. *Sci Rep*. 2018;8:7659. doi:10.1038/s41598-018-25965-w
27. Barnett PR, Hulett BM, et al. Crashworthiness of recycled carbon fiber composites. *Compos Struct*. 2021;272:114232. doi:10.1016/j.compstruct.2021.114232
28. Jia S, Zhou J, Jiang Z. Study on the mechanical performances of carbon fiber/epoxy composite material subjected to dynamical compression and high temperature loads. *Compos Struct*. 2021;258:113421. doi:10.1016/j.compstruct.2020.113421
29. Pittala PK et al. Self-healing of matrix cracking and delamination damage assessment in microcapsules reinforced carbon fiber epoxy composite under flexural loading. *Compos Struct*. 2022;291:115691. doi:10.1016/j.compstruct.2022.115691
30. Jin FL, Li X, Park SJ. Synthesis and application of epoxy resins: a review. *J Ind Eng Chem*. 2015;29:1-11. doi:10.1016/j.jiec.2015.03.026
31. Liu S, Chevali VS, Xu Z, Hui D, Wang H. A review of extending performance of epoxy resins using carbon nanomaterials. *Compos B Eng*. 2018;136:197-214. doi:10.1016/j.compositesb.2017.08.020
32. Ammar MMA, Zhao P, Zhao P, Shi Y. An approach for damage initiation and propagation in metal and carbon fiber hybrid composites manufactured by robotic fiber placement. *Compos Struct*. 2021;268:113976. doi:10.1016/j.compstruct.2021.113976
33. Ryzińska G, David M, Wroński S, et al. Effect of fiber architecture on the specific energy absorption in carbon epoxy composite tubes under progressive crushing. *Compos Struct*. 2019;227:111292. doi:10.1016/j.compstruct.2019.111292
34. Xiong J, Hu H, Wu LZ, et al. Compression behavior and energy absorption of carbon fiber reinforced composite sandwich panels

made of three-dimensional honeycomb grid cores. *Extreme Mech Lett*. 2016;7:114-120. doi:10.1016/j.eml.2016.02.012

35. Zheng Y. *Study on High Modulus Resin Matrix and High Compressive Composites*. Northwestern Polytechnical University; 2002 http://www.cnki.net
36. Zhang BY, Wang W, Wu GH. Dynamic-compression mechanical properties and energy-absorption capability of fly-ash cenospheres-reinforced 1199Al-matrix composite foam. *Explos Shock Waves*. 2014;34:28-34. http://www.cnki.net

How to cite this article: Liang W, Wang L, Liaw PK, Liu Y, Wei R, Xu J. On the energy absorption in a novel CoFeSiB metallic-glass fiber/epoxy resin composite under quasi-static and dynamic compression conditions. *Polym Compos*. 2024;45(6):5290-5299. doi:10.1002/pc.28127.